Check for updates

Advanced Functional Materials

ADVANCED FUNCTIONAL MATERIALS
www.afm-journal.de

RESEARCH ARTICLE

Wireless, Battery-Free, Optoelectronic, Multi-Modal Sensor Integrated With Colorimetric Dressing for Diabetic Ulcer Management

Seokjoo Cho[1,2] | Ji-Hwan Ha[3] | Jiwon Moon[1] | Jihyeon Ahn[1,4] | Gwangmook Kim[2] | Xiaotian Ma[2] | Kexin Fan[2] | Ruihao Song[2] | Donho Lee[1] | Hyeonseok Han[1] | Junseong Ahn[5] | Youngwoo Oh[6] | Wooyeol Choi[7] | Yong Suk Oh[8] | Soonhyoung Hwang[4] | Sohee Jeon[4,9] | Yongrok Jeong[10] | Dahong Kim[4] | Su A. Park[4] | Jun-Ho Jeong[4,11] | Wei Gao[2] | Inkyu Park[1]

[1]Department of Mechanical Engineering, Korea Advanced Institute of Science and Technology, Daejeon, Republic of Korea | [2]Andrew and Peggy Cherng Department of Medical Engineering, Division of Engineering and Applied Science, California Institute of Technology, Pasadena, CA, USA | [3]Department of Mechanical Engineering, Hanbat National University, Daejeon, Republic of Korea | [4]Department of Nano-manufacturing Technology, Korea Institute of Machinery and Materials, Daejeon, Republic of Korea | [5]Department of Control and Instrumentation Engineering, Korea University, Sejong, Republic of Korea | [6]Department of Computer Engineering, College of IT Convergence, Chosun University, Gwangju, Republic of Korea | [7]School of Computer Science and Engineering, Chung-Ang University, Seoul, Republic of Korea | [8]Department of Mechanical Engineering, Changwon National University, Changwon, Republic of Korea | [9]College of Pharmacy, Chung-Ang University, Seoul, Republic of Korea | [10]School of Mechanical Engineering, Kyungpook National University, Republic of Korea | [11]College of Medicine, Chung-Ang University, Seoul, Republic of Korea

Correspondence: Jun-Ho Jeong (jhjeong@kimm.re.kr) | Wei Gao (weigao@caltech.edu) | Inkyu Park (inkyu@kaist.ac.kr)

Received: 16 December 2025 | **Revised:** 4 January 2026 | **Accepted:** 5 January 2026

Keywords: battery-free | colorimetric dressing | diabetic ulcer | electrospinning | optoelectronic | wireless sensor

ABSTRACT

Diabetic ulcers are a severe complication of diabetes, often leading to infection, amputation, and increased mortality. Early detection of diabetic ulcer deterioration requires diagnosis of key biochemical indicators such as pH, glucose, and temperature to prevent wound deterioration and improve patient outcomes. Most traditional wound dressings focus solely on protection and healing but lack the ability to diagnose these critical factors. Here, a wireless, battery-free optoelectronic patch integrated with electrospun colorimetric dressings is introduced for multimodal wound monitoring. The dressing incorporates curcumin–polycaprolactone (C-PCL) and 3,3',5,5'-Tetramethylbenzidine-glucoseoxidase-peroxidase-polycaprolactone (TGP-PCL)-based electrospun fiber, producing distinct colorimetric transitions in response to pH and glucose. These colorimetric diagnostic performances are quantified by measuring reflectance differences under specific wavelength light through integrated LED–photodiode pairs, respectively. Furthermore, the wireless, battery-free sensor enables continuous, real-time monitoring without causing discomfort to the patient, offering both qualitative visual feedback and quantitative data for precise self-monitoring. In vivo validation in a rat wound model demonstrated reliable detection of infection-driven alkalization, monitoring of wound temperature, and accurate glucose quantification consistent with a commercial glucometer. This platform merges intuitive visual cues with quantitative electronic outputs in a battery-free, wireless design, offering a practical and cost-effective solution for real-time and multimodal wound monitoring.

Seokjoo Cho and Ji-Hwan Ha contributed equally to the work.

© 2026 Wiley-VCH GmbH

1 | Introduction

Diabetic ulcers represent one of the most severe complications of diabetes, affecting 15%–34% of patients during their lifetime and frequently leading to infection, amputation, and elevated mortality [1–3]. With an aging global population, the prevalence of diabetic ulcers continues to rise, further amplifying this clinical and socioeconomic burden. These wounds lead to high treatment expenses and serious impacts on social and economic well-being, with annual treatment costs in the United States estimated at nearly $13 billion [4–6]. As diabetic ulcer progresses, even minor wounds may fail to heal, eventually leading to ulceration [2]. In severe cases, poor blood circulation can result in tissue necrosis, making recovery difficult [7, 8]. Once developed, diabetic ulcers are difficult to heal and prone to recurrence, increasing the risk of severe infection and further complications. Clinical staging systems classify diabetic ulcer into five or six progressive stages [3, 9, 10]. (Figure S1) In the early stages (0–1), when only superficial changes or pre-ulcerative lesions appear, biochemical detection remains difficult. From stage 2 onward, once dermal tissue becomes exposed and the risk of infection rises, biochemical indicators such as pH, glucose, and temperature provide clinically relevant insights into wound deterioration. Wound alkalization reflects bacterial growth [11–14], elevated glucose levels impair healing [15, 16], and local temperature changes signal inflammation or infection [17, 18], highlighting the importance of multimodal biochemical monitoring.

As diabetic ulcers often progress into chronic wounds, they require long-term, day-to-day management and multimodal biochemical assessment to prevent further deterioration [19–21]. However, current diagnostic approaches remain insufficient for early intervention. Pinprick tests and sensory evaluations provide limited accuracy and lack capability for continuous monitoring [22, 23]. Imaging modalities such as radiography and ultrasound improve diagnostic precision but require costly equipment and medical expertise, restricting accessibility [24–26]. Routine wound care still relies heavily on visual inspection and intermittent laboratory testing, which are subjective, invasive, and inadequate for real time monitoring.

Recent progress in advanced wound dressings [27–42] and wearable sensors [43–49] has aimed to overcome these limitations. Colorimetric dressings offer a simple and low-cost means of visualizing biochemical changes via color shifts [36–40]. However, their reliance on naked-eye evaluation limits quantitative accuracy and hinders continuous assessment. Camera based readouts provide quantitative data but require bulky hardware and significant power, reducing practicality for daily use [28, 29, 50]. Recently, AI-based colorimetric quantification methods have been introduced to improve analytical accuracy [43, 51]. However, these approaches rely heavily on post-processing, thereby diminishing the inherent intuitiveness and simplicity of colorimetric sensing. Optical sensing platforms that directly integrate with colorimetric materials have shown promise by enabling accurate state detection without cameras or post-processing, though most remain confined to proof-of-concept demonstrations [41]. Moreover, colorimetric sensing for diabetes-related biomarkers has rarely been translated into dressing or fiber-based wound systems, leaving a critical technological gap.

Meanwhile, wireless sensors have transformed real-time physiological monitoring at the skin interface [47, 44, 49, 52–55]. Near-field communication (NFC) based platforms in particular enable battery-free operation, miniaturization, and seamless data transfer to external devices, making them highly attractive for wound diagnostics [41, 49, 56–61]. Integration of such sensors with wound dressings that also protect the wound and promote healing presents an advanced approach to comprehensive wound management.

In this study, a wireless, battery-free optoelectronic patch integrated with electrospun colorimetric dressings is introduced for multimodal monitoring of wound biomarkers, including pH, glucose, and temperature. Functional electrospun fibers were engineered through composite fiberization to enable colorimetric readouts for both pH and glucose. Although pH-responsive colorimetric fibers have been widely investigated, this work presents the first realization of glucose-indicative fibers exhibiting a visible color change. The dressing incorporates curcumin–polycaprolactone (C-PCL) and TMB–glucose oxidase–peroxidase–polycaprolactone (TGP-PCL), each producing distinct visible colorimetric transitions responsive to pH and glucose. These optical shifts are quantitatively captured by integrated LED–photodiode pairs, while a thermistor monitors wound temperature. A flexible NFC-based circuit enables wireless power harvesting and data transmission, and a packaging layer composed of polydimethylsiloxane (PDMS), black dye, and polyethyleneimine ethoxylated (PEIE) ensures strong adhesion and mechanical robustness. The functionality of this platform was validated in a rat wound model, demonstrating reliable in vivo monitoring of infection-driven alkalization, wound temperature, and systemic glucose levels. By integrating visual feedback with quantitative electronic readouts, the system provides both patients and clinicians with actionable wound information for early intervention and prevention of diabetic ulcer complications. This platform offers a practical, user-friendly solution for rapid and quantitative assessment of diabetic wounds in daily life, offering an accessible approach to timely care and complication prevention.

2 | Results and Discussion

2.1 | Overview of the Integrated Wireless Colorimetric Sensing System

To enable the prevention and early diagnosis of diabetic ulcers, this study proposes a development of a wireless, battery-free, multi-modal sensor system integrated with a colorimetric diagnostic electrospun fibers-based wound dressing for continuous monitoring of key biomarkers—glucose, pH, and temperature. Although various colorimetric sensors have been reported (Table S1), most rely on detecting a single analyte, such as pH or bacteria, and often lack the capability to simultaneously monitor multiple physiological parameters essential for comprehensive wound assessment. Furthermore, existing platforms typically struggle to integrate these sensing modalities into a unified, wearable format without compromising mechanical flexibility or requiring complex external equipment. The system combines advanced wound management with real-time, non-invasive sensing of these critical biomarkers, allowing for early detection of wound

16163028, 2026, 25, Downloaded from https://advanced.onlinelibrary.wiley.com/doi/10.1002/adfm.202532167 by Korea University Library, Wiley Online Library on [29/03/2026]. See the Terms and Conditions (https://onlinelibrary.wiley.com/terms-and-conditions) on Wiley Online Library for rules of use; OA articles are governed by the applicable Creative Commons License

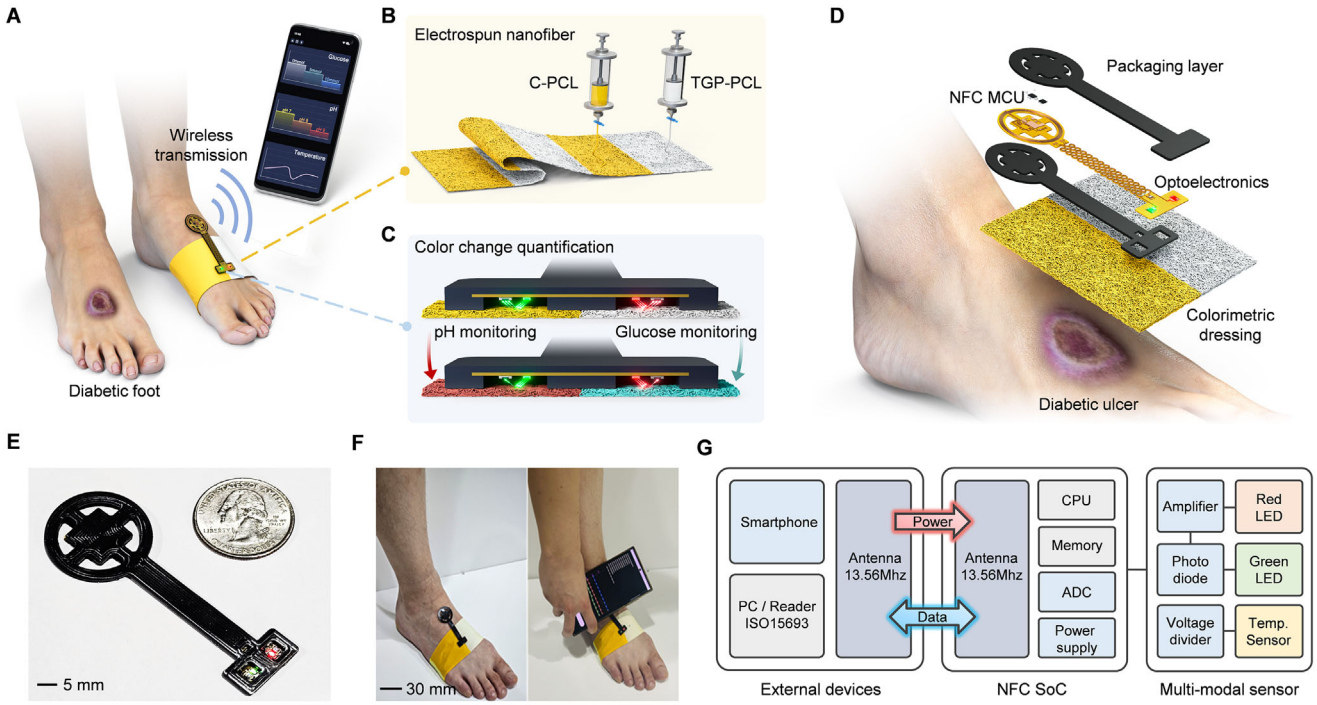


FIGURE 1 | Wireless, battery-free multi-modal sensor system for continuous diabetic ulcer monitoring. (A) Conceptual illustration of the wireless battery-free system integrated with a PCL-based dressing for real-time wound monitoring. (B) Electrospun nanofiber fabrication of C-PCL and TGP-PCL composites. (C) Cross-sectional schematic of optoelectronic modules for quantifying dressing color changes with pH and glucose. (D) Exploded view of the integrated platform with packaging, NFC MCU, and optoelectronics layered on the colorimetric dressing. (E) Photograph of the after packaging compared with a quarter coin. (F) On-body demonstration with smartphone readout. (G) Block diagram illustrating external NFC devices, NFC SoC, and multi-modal sensors.

deterioration and potential complications. A wireless, battery-free, multimodal sensing platform integrates an optoelectronic module with functional colorimetric dressings to enable continuous and non-invasive monitoring of diabetic ulcers. This platform operates through near-field communication (NFC), harvesting power and transmitting data directly to external devices such as smartphones. (Figure 1A) This design reduces device size, improves patient comfort, and enhances clinical practicality by enabling quantitative analysis in conditions where direct visual inspection of colorimetric changes is restricted, such as during shoe wearing or cast immobilization.

Electrospun nanofiber dressing provide the functional interface for biomarker monitoring. Curcumin–polycaprolactone (C-PCL) nanofibers exhibit antimicrobial activity and undergo a pH-dependent shift from yellow to red, while 3,3',5,5'-Tetramethylbenzidine-Glucoseoxidase-Peroxidase-Polycaprolactone (TGP-PCL) nanofibers detect glucose through enzymatic oxidation and peroxidase-mediated conversion of 3,3',5,5'-tetramethylbenzidine (TMB), producing a white-to-navy change. Parallel electrospinning produces spatially distinct but integrated sensing regions within a single dressing (Figure 1B).

Quantification of these colorimetric changes is achieved by integrated optoelectronic readout, where LED–photodiode pairs measure reflectance corresponding to local biomarker levels. This strategy allows compact and robust signal acquisition without the need for bulky cameras, ensuring compatibility with wireless operation. A green LED and PD system monitors the pH-induced yellow-to-red color shifts in the C-PCL dressing, while a red LED and PD system tracks the glucose-related white-to-navy transitions in the TGP-PCL dressing. These color changes are quantified by analyzing the reflectance of light from the dressing surface. (Figure 1C) In addition to colorimetric sensing, the system integrates a temperature monitoring component using a thermistor. The thermistor, connected to a voltage divider circuit, allows for accurate measurement of temperature changes within the wound environment, which are essential for detecting inflammation or infection. The temperature sensing is independent of the optoelectronic system and is quantified through electrical resistance changes corresponding to variations in temperature, providing a direct, real-time readout of wound conditions. All biomarker data, including colorimetric shifts and temperature readings, are transmitted wirelessly via an NFC-based communication system, enabling continuous, battery-free monitoring. A multilayer assembly combines the NFC antenna, microcontroller, and signal-conditioning circuits with the nanofiber dressing, forming a flexible patch that conforms to skin and maintains intimate contact with ulcer tissue.

The packaging layer is laminated above and below the flexible printed circuit board (fPCB), shielding the optoelectronic components from ambient light and mechanical disturbances while serving as an adhesive layer between the electronics and the dressing for stable monitoring. (Figure 1D) Figure 1E presents a flipped-over view of the fabricated patch next to a quarter coin, underscoring its compact footprint. On-body demonstrations confirm conformal adhesion to the foot and

16163028, 2026, 25, Downloaded from https://advanced.onlinelibrary.wiley.com/doi/10.1002/adfm.202532167 by Korea University Library, Wiley Online Library on [29/03/2026]. See the Terms and Conditions (https://onlinelibrary.wiley.com/terms-and-conditions) on Wiley Online Library for rules of use; OA articles are governed by the applicable Creative Commons License

real-time wireless transmission of biomarker data to a smartphone interface (Figure 1F). A system-level block diagram illustrates wireless power harvesting at 13.56 MHz, data digitization by the microcontroller and Analog-to-Digital Converter (ADC), and transmission of processed outputs from the photodiodes and thermistor (Figure 1G). This data can be accessed in real time on a mobile device, providing both visual feedback through the color changes and quantitative diagnostic data from the sensors.

Furthermore, the system is designed with a modular architecture, in which the colorimetric dressing serves as a disposable, single-use component, while the wireless optoelectronic patch is reusable. The dressing supports continuous wound monitoring for up to approximately one month, after which it can be replaced without discarding the electronic module. The wireless patch is physically separated from the dressing and can be repeatedly reused after simple surface sanitization, enabling a cost-effective replacement strategy. As detailed in Table S2, the materials and fabrication processes allow the wireless patch to be produced at low cost, enhancing its translational potential for long-term clinical use. This integrated approach offers a practical, user-friendly solution for diabetic ulcers management, enabling timely interventions and reducing the risk of severe complications.

2.2 | Basic Characteristic of Electrospun Colorimetric Wound Dressing

Electrospun nanofiber dressings based on TGP–PCL and C–PCL were characterized to evaluate their morphological, chemical, and biological properties (Figure 2). These functional electrospun dressing consisted of spatially separated regions of TGP–PCL and C–PCL, as shown in the photograph (Figure 2A). Although pH-responsive fiberization of C-PCL has been advanced in prior studies [38, 40, 41], its application has largely been limited to single-analyte colorimetric dressings or standalone sensors. To achieve multimodal sensing of the diabetic-ulcer microenvironment within a single dressing, TGP-PCL, a composite that provides glucose-responsive colorimetry was integrated with C-PCL through a continuous electrospinning process. By combining the two via an electrospinning process, a unified multimodal colorimetric dressing was successfully produced. The two colorimetric nanofiber dressings were produced as a single, continuous construct in which the TGP–PCL and C–PCL composites were seamlessly joined on one dressing sheet. Detailed fabrication procedures are described in the Methods section, and the overall process is illustrated in Figure S2. Figure 2B–D illustrates the key characteristics of TGP-PCL, while Figure 2E–G focus on the characteristics of C-PCL. Figure 2B presents scanning electron microscopy (SEM) images of the electrospun TGP-PCL nanofibers, which exhibit a random orientation. The fibers have an average diameter of 843 nm with a standard deviation of 78 nm, within a range of 400–1200 nm (Figure 2C). As shown in Figure S3, TGP-PCL and C-PCL integrated dressings were successfully fabricated over a large area ($> 30\,cm \times 30\,cm$). This result confirms the feasibility of large-area production using electrospinning. Figure S4 compares the tensile stress–strain behavior of TGP-PCL and C-PCL under dry and wet conditions. In the dry state, TGP-PCL exhibited a high elongation at break of 371% and an ultimate tensile strength of 1.43 MPa. In contrast, C-PCL showed a significantly higher stiffness and strength, with an ultimate tensile strength of 2.95 MPa, but a much lower elongation at break of approximately 69%. Accordingly, the Young's modulus of C-PCL was estimated to be notably higher (85.34 MPa) compared to that of TGP-PCL (5.58 MPa), confirming that the incorporation of curcumin acts as a rigid reinforcement within the polymer matrix. Upon hydration, the mechanical responses of the materials diverged interestingly. For TGP-PCL (wet), the ultimate tensile strength increased remarkably to 2.50 MPa, while the elongation at break slightly decreased to 281% compared to its dry state. On the other hand, C-PCL (wet) displayed a dramatic transformation in ductility; while maintaining a high ultimate tensile strength of 2.93 MPa, its elongation at break surged to 691%. To confirm the composition of TGP-PCL, Fourier transform infrared (FTIR) spectroscopy was conducted (Figure 2D). The analysis revealed the presence of an OH stretch (3400–3600 cm^{-1}) and Amide I bands (1640–1660 cm^{-1}), corresponding to GOx, peroxidase, and TMB in the TGP-PCL, along with the identification of alkane chains (2945–2845 cm^{-1}) and C═O ester groups (1720 cm^{-1}) from PCL. Figure 2E presents SEM images of the electrospun C-PCL nanofibers, also exhibiting a random orientation. These fibers have a smaller average diameter of 143 nm, with a standard deviation of 59 nm and a range of 20–400 nm (Figure 2F). The base PCL contents is identical in TGP-PCL and C-PCL colorimetric fibers; however, their diameters differ owing to the distinct loadings of components used to preserve colorimetric performance. FTIR analysis (Figure 2G) confirmed the presence of an OH stretch (3400–3600 cm^{-1}) associated with curcumin in C-PCL, along with alkane chains (2945–2845 cm^{-1}) and C═O ester groups (1720 cm^{-1}) from PCL. Collectively, these analyses confirm that the multi-composite PCL dressings form randomly intertwined nanofiber networks with high porosity, which benefit air permeability and wound healing by the gas exchange from the wound. The air permeability of TGP-PCL and C-PCL was measured as 7.13 and 6.23 $cm^3\ cm^{-2}\ s^{-1}$, respectively, values that lie between those of denim (3.41 $cm^3\ cm^{-2}\ s^{-1}$) and cotton (7.82 $cm^3\ cm^{-2}\ s^{-1}$) (Figure S5).

Biocompatibility was validated through fibroblast cell (NIH 3T3) culture studies. SEM imaging demonstrated progressive cellular proliferation on both composites over days 1, 4, and 7 (Figure 2H). Quantitative OD measurements at 440 nm confirmed significantly enhanced growth compared to pristine PCL, with C–PCL exhibiting the strongest proliferation, consistent with the bioactivity of curcumin (Figure 2I). In addition, antimicrobial evaluation confirmed that both composites suppress bacterial growth, with strong activity against *Staphylococcus aureus* and *Escherichia coli* (Figure 2J). Representative agar plate images in Figure S6 further illustrate the bactericidal effect of C–PCL and the partial suppression provided by TGP–PCL. In C-PCL, pronounced antibacterial activity derives from the high polyphenol content of curcumin, whereas in TGP-PCL it arises from the generation of reactive oxygen species.

Together, these results establish that the electrospun TGP-PCL and C-PCL dressings combine structural integrity, chemical functionality, biocompatibility, and antimicrobial activity, thereby supporting their use as multifunctional wound dressings for diabetic ulcer management.

16163028, 2026, 25, Downloaded from https://advanced.onlinelibrary.wiley.com/doi/10.1002/adfm.202532167 by Korea University Library, Wiley Online Library on [29/03/2026]. See the Terms and Conditions (https://onlinelibrary.wiley.com/terms-and-conditions) on Wiley Online Library for rules of use; OA articles are governed by the applicable Creative Commons License

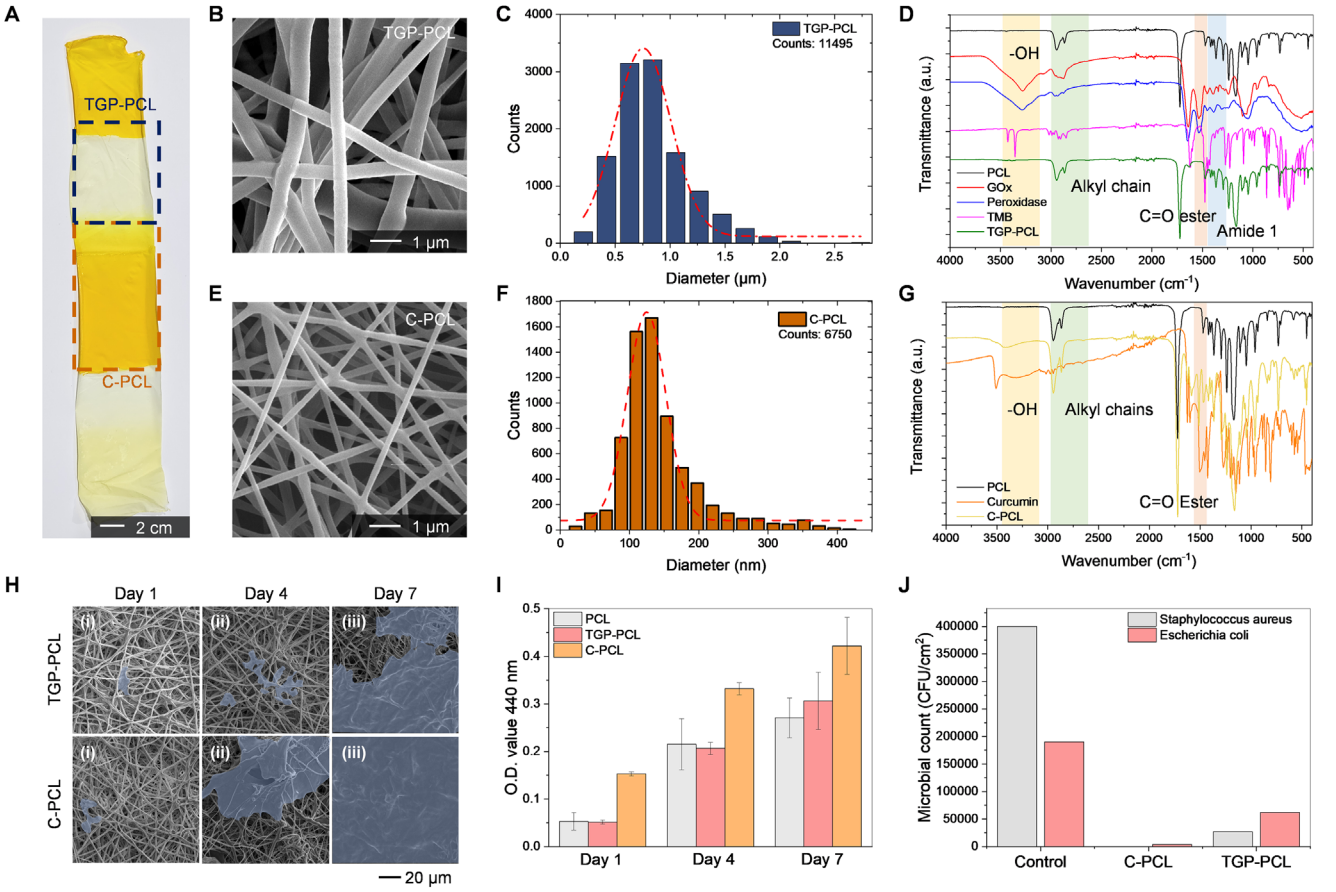


FIGURE 2 | Characteristics of electrospun TGP-PCL and C-PCL dressings. (A) Photograph of TGP-PCL & C-PCL nanofiber dressings. (B) SEM image of electrospun TGP-PCL fibers. (C) Distribution of electrospun TGP-PCL nanofiber diameters (average diameter: 843 nm, standard deviation: 78 nm, analysis area: 100 μm^2, counts: 11495). (D) FTIR analysis of PCL, curcumin, and TGP-PCL (OH stretching: 3400–3600 cm^{-1}, Alkyl chain: 2945–2845 cm^{-1}, C═O ester: 1720 cm^{-1}, Amide I: 1640–1660 cm^{-1}). (E) SEM image of electrospun C-PCL fibers. (F) Distribution of electrospun C-PCL nanofiber diameters (average diameter: 143 nm, standard deviation: 59 nm, analysis area: 100 μm^2, counts: 6750). (G) FTIR analysis of PCL, curcumin, and C-PCL (OH stretching: 3400–3600 cm^{-1}, Alkyl chain: 2945–2845 cm^{-1}, C═O ester: 1720 cm^{-1}). (H) SEM images of cell proliferation on TGP-PCL and C-PCL at days 1, 4, and 7. (I) Quantification of cell proliferation by OD values at 440 nm, showing enhanced growth on both composites, with C-PCL outperforming pristine PCL. (J) Antimicrobial properties of C-PCL and TGP-PCL against *Staphylococcus aureus* and *Escherichia coli*.

2.3 | Mechanism and Quantitative Optoelectronic Readout of Colorimetric Dressings

Figure 3A,B provides a cross-sectional view of the sensor, demonstrating its working mechanism based on color changes in the dressings and the corresponding shifts in light reflectance at varying glucose and pH levels. The sensor functions on the principle that color is perceived through the absorption and reflection of light across specific wavelengths. Red and green LEDs, positioned at the base of the NFC patch, are used to illuminate the TGP-PCL and C-PCL dressings, respectively. As the dressings undergo color changes, the corresponding variations in light reflectance are detected by individual photodiodes. As glucose levels rise at the skin interface, indicative of diabetes progression, the TGP-PCL dressing transitions from white to navy (0–10 mmol, 7 mmol: diabetic ulcer glucose concentration). This color shift reduces the reflectivity of red light, resulting in a lower amount of light being captured by the photodiode. (Figure 3A) Similarly, as the pH of a chronic wound increases due to bacterial infection, the C-PCL dressing changes from yellow to red, which decreases the reflectivity of green light and leads to a reduction in light detected by the corresponding photodiode. (Figure 3B) Figure 3C,D shows the photographs of colorimetric dressings under different target concentrations. Figure 3C shows the visual transition of the TGP-PCL dressing, changing from white to dark navy as glucose concentration rises. Figure 3D depicts the color changes in the C-PCL dressing, shifting from yellow at neutral pH to dark yellow at pH 7, orange at pH 8, and red at pH 9. In the electrospun TGP-PCL dressing, TMB, GOx, and HRP are consist within the fiber matrix. Glucose is oxidized by GOx to gluconic acid with concomitant H_2O_2 formation, which HRP uses to oxidize TMB to its blue/navy diimine/cation-radical state, producing a glucose-dependent chromatic shift. Figure 3E shows the reaction mechanism of glucose oxidation and subsequent TMB conversion catalyzed by GOx and peroxidase and its oxidation behavior under varying glucose levels. Under the catalysis of GOx, glucose is oxidized to produce hydrogen peroxide, which further reacts with TMB, catalyzed by peroxidase, resulting in the formation of blue ox-TMB, whereas curcumin in the C-PCL composite undergoes hydrogen dissociation under alkaline conditions, producing red-shifted chromophores. (Figure 3F) The colorimetric transitions of both colorimetric dressings are further validated by mapping

16163028, 2026, 25, Downloaded from https://advanced.onlinelibrary.wiley.com/doi/10.1002/adfm.202532167 by Korea University Library, Wiley Online Library on [29/03/2026]. See the Terms and Conditions (https://onlinelibrary.wiley.com/terms-and-conditions) on Wiley Online Library for rules of use; OA articles are governed by the applicable Creative Commons License

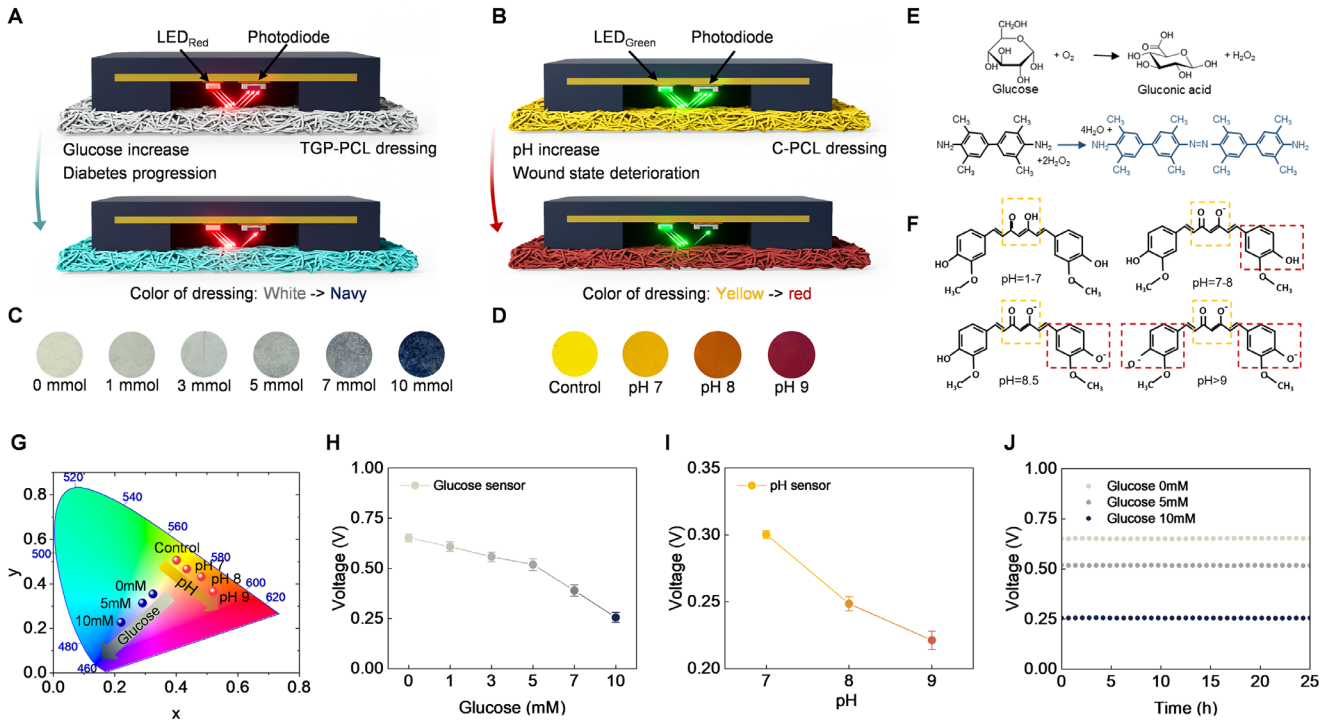


FIGURE 3 | Working mechanism and quantitative colorimetric sensing using optoelectronic modules. (A–B) Working mechanism of quantitative sensing principle with colorimetric dressing: (A) TGP-PCL based glucose sensor. (B) C-PCL based pH sensor. (C) Photographs of TGP-PCL dressings under glucose concentrations from 0 to 10 mM. (D) Photographs of C-PCL dressings at pH 7–9. (E) Reaction mechanism of glucose oxidation and TMB conversion in the TGP–PCL dressing according to glucose levels (0, 1, 3, 5, 7, and 10 mmol). (F) Structure changes of curcumin in the C-PCL dressing according to pH levels (pH 7, 8, and 9). (G) CIE 1931 color space mapping of glucose- and pH-dependent transitions. (H) Voltage response of the glucose sensor, showing concentration-dependent decreases in red reflectance. (I) Voltage response of the pH sensor, showing pH-dependent decreases in green reflectance. (J) Stability of glucose sensor output over 24 h.

into the CIE 1931 color space (Figure 3G), which demonstrates clear, quantifiable shifts from white to navy for glucose and from yellow to red for pH. To further quantify these visual changes, standardized image analysis was performed. The pH dressing exhibited a monotonic decrease in the green value (sRGB_G) with increasing pH, while the glucose dressing showed a concentration-dependent decrease in the red value (sRGB_R) (Figure S7). This direct correspondence between biomarker concentration and specific color values validates the strategy of assigning a single optimized wavelength to each sensing modality. Integration with the optoelectronic system enabled these visual changes to be translated into electronic signals. For glucose sensing, increasing concentrations from 0 to 10 mM produced a progressive reduction in red reflectance, which translated into a stepwise decrease in photodiode voltage (Figure 3H). Similarly, for pH sensing, the gradual transition of C–PCL from yellow to red corresponded to a monotonic reduction in green reflectance, yielding a consistent decline in voltage output across pH 7–9 (Figure 3I). These results confirm that the system achieves reliable optical-to-electrical conversion, eliminating the subjectivity of visual inspection and enabling real-time, quantitative monitoring. The operational stability of the device was further validated through continuous testing of the glucose sensor over a 24 h period. Voltage outputs at 0, 5, and 10 mM glucose remained stable without noticeable drift or signal degradation, underscoring the robustness of the wireless, battery-free system for prolonged monitoring (Figure 3J). This stability highlights the potential for deployment in clinical settings where long-term wound monitoring is required. In addition to demonstrating operational stability, the sensitivity of the optical readout could be modulated by adjusting the bottom encapsulation thickness, which determines the distance between the LED–photodiode pair and the dressing. Thinner encapsulation enhanced the response magnitude, and the pH sensor exhibited the largest voltage differences at 0.5 mm. Thicker layers (1.0–2.0 mm) reduced the overall sensitivity but maintained detectable responses (Figure S8). These results highlight encapsulation thickness as a tunable design parameter for optimizing sensing performance. Together, these results demonstrate that the colorimetric dressings provide reliable, concentration-dependent responses to glucose and pH, and that integration with optoelectronics enables quantitative electronic readouts, establishing a practical platform for wound biomarker monitoring.

2.4 | Design and Packaging of the Wireless Battery-Free Patch

Figure 4A illustrates a schematic of the wireless, battery-free optoelectronic patch with a multimodal sensing module for monitoring key risk factors of diabetic ulcers. The patch includes an NFC circuit for wireless communication and power supply, an optoelectronic unit for glucose and pH monitoring, and a thermistor for temperature sensing. The entire device is encapsulated in PDMS infused with black dye to protect it from external light interference and physical stimuli. The NFC circuit

16163028, 2026, 25, Downloaded from https://advanced.onlinelibrary.wiley.com/doi/10.1002/adfm.202532167 by Korea University Library, Wiley Online Library on [29/03/2026]. See the Terms and Conditions (https://onlinelibrary.wiley.com/terms-and-conditions) on Wiley Online Library for rules of use; OA articles are governed by the applicable Creative Commons License

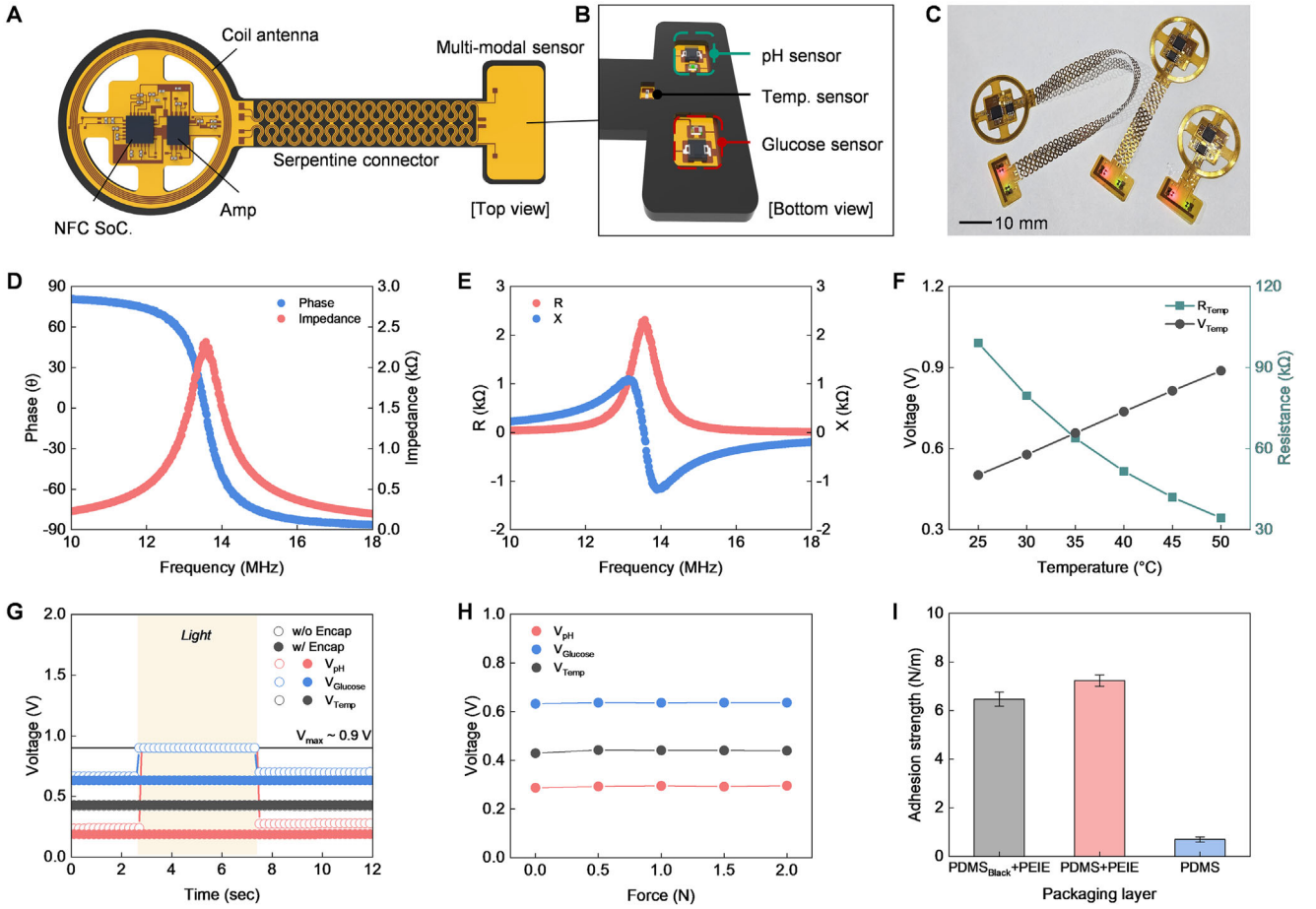


FIGURE 4 | Design and characterization of the wireless, battery-free NFC patch. (A) Schematic of the integrated patch consisting of an NFC SoC, coil antenna, op-amp, and multi-modal sensing unit with optoelectronics and thermistor, encapsulated in PDMS infused with black dye. (B) Bottom view schematic showing glucose, pH, and temperature sensors integrated on the fPCB. (C) Photograph of flexible NFC patches with serpentine interconnectors of varying lengths, enabling conformal attachment at different foot locations. (D) Phase and impedance spectra of the NFC antenna, confirming resonance at 13.56 MHz. (E) Resistance and reactance characteristics showing optimized tuning for efficient power harvesting. (F) Calibration curve of the thermistor-based temperature sensor (25–50°C). (G) Real-time voltage responses of glucose, pH, and temperature sensors under light illumination with and without encapsulation. (H) Mechanical stability of voltage signals under external force. (I) Adhesion strength of different packaging strategies, with PDMS + PEIE showing improved durability.

is composed of an NFC system-on-chip (SoC), an operational amplifier (op-amp), and a coil antenna mounted on the front side of a fPCB. On the reverse side of the fPCB, optoelectronic components, including photodiodes, a red LED for detecting glucose-induced color changes in the TGP–PCL dressing, a green LED for detecting pH-induced changes in the C–PCL dressing, and the thermistor. (Figure 4B) To enhance breathability and allow the biofluids from the dressing to pass through, the fPCB is designed with through-holes between the coil and circuit areas. The circuit section containing the coil and NFC SoC is connected to the sensing section through a serpentine interconnector, which accommodates mechanical deformation and enables conformal attachment to various locations on the foot. The serpentine layout can also be fabricated with variable lengths, allowing the patch to be customized and positioned according to the user's clinical needs or wound location. (Figure 4C)

The antenna exhibited a clear and stable resonance at 13.56 MHz, the designated frequency for NFC operation. Figure 4D shows the phase and impedance spectra, which demonstrate sharp resonance behavior with well-matched impedance near the operating frequency. This optimized electrical response confirms efficient coupling between the antenna coil and the NFC SoC, minimizing mismatch losses and ensuring reliable wireless communication. Figure 4E further shows the resistance and reactance characteristics of the antenna. The resistance remained low around resonance, while the reactance crossed zero precisely at 13.56 MHz, validating the correct tuning of the coil antenna. To examine the tunability of the antenna design, a parametric analysis was conducted by varying the matching capacitance while maintaining a fixed antenna geometry. As shown in Figure S9, systematic shifts in the resonant frequency were observed with different capacitance values, consistent with LC resonance behavior.

Such characteristics are critical for maximizing wireless power harvesting efficiency, reducing energy dissipation, and maintaining signal integrity during operation. To further evaluate the practical wireless operating range, the maximum communication distance between the wireless patch and the external antenna was

16163028, 2026, 25, Downloaded from https://advanced.onlinelibrary.wiley.com/doi/10.1002/adfm.202532167 by Korea University Library, Wiley Online Library on [29/03/2026]. See the Terms and Conditions (https://onlinelibrary.wiley.com/terms-and-conditions) on Wiley Online Library for rules of use; OA articles are governed by the applicable Creative Commons License

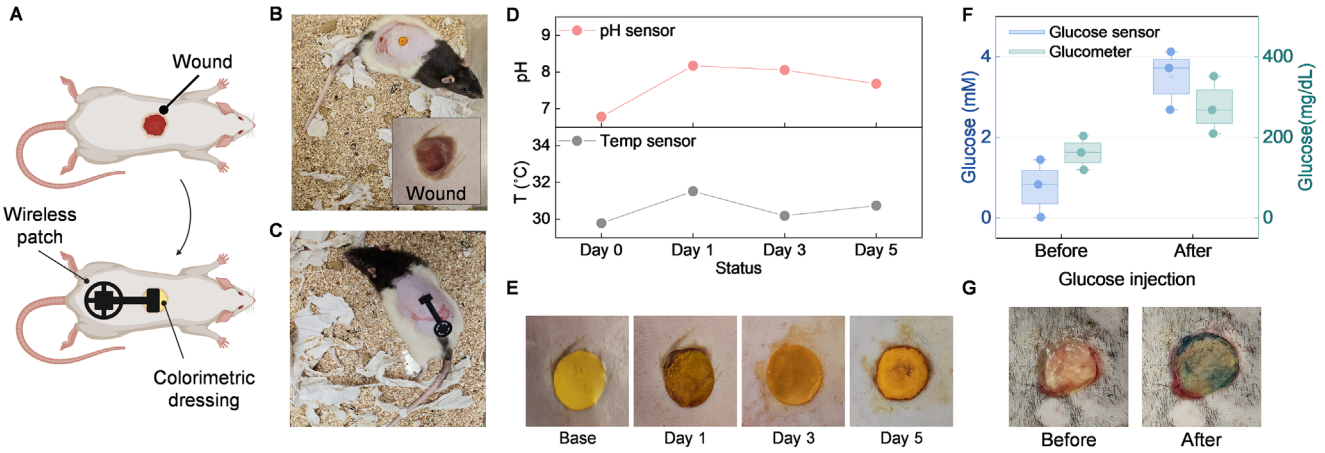


FIGURE 5 | In vivo multimodal biomarker monitoring with a wireless, battery-free optoelectronic patch integrated with colorimetric dressings. (A) Schematic representation of the rat model with the wireless, battery-free patch with colorimetric dressing applied for in vivo wound monitoring. (B) Photographs of rats with pH-sensitive dressing. (C) Photograph of a rat with the integrated wireless patch applied over the wound site. (D) Real-time monitoring of wound pH and temperature over 5 days, showing increased alkalinity during wound progression. (E) Sequential images of pH-responsive dressings at baseline and at days 1, 3, and 5, showing progressive color changes associated with wound state. (F) Glucose concentration changes measured by the integrated patch compared with a commercial glucometer before and after glucose injection. (G) Photographs of glucose dressing before and after glucose injection, confirming visible colorimetric transition.

experimentally characterized. As shown in Figure S10, stable NFC operation was maintained as the separation distance increased along the normal (Z) direction, demonstrating reliable wireless communication within the experimentally validated operating range.

Figure 4F shows the characteristics of the Negative Temperature Coefficient (NTC) thermistor under different temperature levels. The NTC thermistor displays a decrease in resistance as external temperature increases, resulting in a voltage output that rises linearly over time when integrated into a circuit such as a voltage divider. For stable sensor performance, it is essential that its response remains consistent, unaffected by external environmental conditions. To evaluate cross-sensitivity, transient heating (~ 100°C) was applied using a heat gun. Only the temperature sensor responded significantly, while glucose and pH modules remained unaffected. (Figure S11) These results confirm selective thermal sensitivity of the thermistor and thermal robustness of the optoelectronic sensors. Figure 4G shows the effect of external light interference on sensor stability. Without the black PDMS packaging, the sensor's output increased due to external light interference. However, with the PDMS packaging, the sensor's response remained steady and unaffected by external light exposure. Mechanical stability tests confirmed that sensor signals remained unaffected under increasing external force (~ 2.0 N) (Figure 4H), highlighting robust device performance under physical stress. Supplementary analysis quantified the voltage response, confirming that variations remained within a few mV and validating the robustness of the patch under physical stress (Figure S12).

The packaging layer is designed using a mixture of PDMS, black dye, and PEIE to ensure strong adhesion to the dressing. (Video S1) As shown in Figure S13, peel tests evaluated the adhesion stability of the encapsulation layers to confirm reliable sensor operation during continuous wear. Figure 4I and Figure S14 present peel test results of the adhesion between the packaging layer and the dressing. The packaging layer composed of PDMS-black and PEIE exhibits an adhesion strength of 6 N mm^{-1}, surpassing that of conventional PDMS. This enhanced adhesion enables the device to remain securely attached to the human body during walking and running, thereby maintaining stable contact with the wound site (Video S2).

2.5 | In Vivo Validation of the Wireless, Battery-Free Patch

The wireless, battery-free patch was evaluated in a rat wound model to demonstrate its in vivo feasibility (Figure 5A). A 10 mm full-thickness wound was surgically created on the dorsal region, and the defect was fully covered with either a pH- or glucose-responsive colorimetric dressing, applied alone or in combination with the wireless patch. To mimic an infected environment, 50 μL of Escherichia coli suspension (10^6 CFU mL^{-1}) was applied to the wound site immediately after injury. Photographs show the rat wound model with a pH-sensitive dressing applied alone (Figure 5B) and with the dressing integrated into the wireless patch (Figure 5C), confirming that the device adhered securely to the skin surface without detachment throughout the study. Time-course monitoring demonstrated the ability of the patch to track wound pH and temperature over five days. The pH sensor revealed a progressive increase in alkalinity from baseline to day 5, reflecting bacterial colonization and impaired healing induced by *E. coli* infection (Figure 5D). In parallel, the thermistor recorded minor variations in wound temperature, which remained within a narrow range of 30–32°C. Sequential images of the pH-responsive dressing confirmed these observations, showing a visible yellow-to-red color shift corresponding to wound alkalization (Figure 5E). Glucose sensing performance was further evaluated using intraperitoneal injection of glucose solution at a dose of 2 g kg^{-1} body weight. The wireless

16163028, 2026, 25, Downloaded from https://advanced.onlinelibrary.wiley.com/doi/10.1002/adfm.202532167 by Korea University Library, Wiley Online Library on [29/03/2026]. See the Terms and Conditions (https://onlinelibrary.wiley.com/terms-and-conditions) on Wiley Online Library for rules of use; OA articles are governed by the applicable Creative Commons License

patch detected a marked increase in glucose concentration after injection, closely matching values obtained from a commercial glucometer (Figure 5F). Concurrently, the TGP–PCL glucose dressing underwent a clear white-to-navy transition (Figure 5G), confirming the enzymatic reaction and the associated electronic signal. Figure S15 further validates the stability of the temperature sensor, showing that the measured wound surface temperature remained nearly constant before and after glucose injection. Together, these in vivo results demonstrate that the wireless, battery-free patch integrated with colorimetric dressings enables multimodal monitoring of wound biochemistry, including pH, temperature, and glucose. The ability to capture infection-driven alkalization and to track systemic glucose levels establishes the platform as a promising tool for translational diabetic ulcer management.

3 | Conclusions

This study presents a wireless, battery-free optoelectronic patch integrated with colorimetric dressings for multimodal monitoring of key biomarkers in diabetic ulcer. The platform combines the intuitive visual feedback of colorimetric dressings with quantitative optoelectronic readouts, enabling both patients and clinicians to access real-time information on wound status. The system captures colorimetric shifts through integrated red and green LEDs and photodiodes for precise glucose and pH measurement, while a thermistor monitors wound temperature. An NFC circuit provides wireless power harvesting and data transmission, ensuring a battery-free design suitable for practical deployment.

The packaging layer, composed of PDMS with black dye and PEIE, demonstrated strong adhesion to the dressing, ensuring that the sensor remains securely attached to the wound site even under mechanical stress. The sensor exhibited stable performance under various environmental challenges, including external temperature changes and light interference, confirming its robustness for real-world application. In vivo validation in a rat wound model demonstrated reliable detection of infection-driven alkalization, stable monitoring of wound temperature, and accurate quantification of glucose levels consistent with a commercial glucometer.

Collectively, these findings establish the wireless, battery-free optoelectronic patch as a practical and cost-effective solution for multimodal wound monitoring. By integrating visual and quantitative feedback, the technology enables continuous, non-invasive assessment of wound biochemistry, supporting early intervention and reducing the risk of severe complications associated with diabetic foot ulcers.

4 | Methods

4.1 | Materials

Polycaprolactone (PCL), 3,3′,5,5′-tetramethylbenzidine (TMB), glucose oxidase (GOx), and horseradish peroxidase (HRP) were purchased from Sigma-Aldrich. N,N-dimethylformamide (DMF) and dichloromethane (DCM) were purchased from Ducksan chemical (Korea).

4.2 | Fabrication of Electrospun Functional Dressing

TGP-PCL dressings were prepared by dissolving PCL (20 wt %) in a 1:1 (v/v) mixture of N,N-dimethylformamide (DMF) and dichloromethane (DCM). Uniform dispersions of 3,3′,5,5′-tetramethylbenzidine (TMB, 8 wt% relative to PCL), glucose oxidase (GOx, 8 wt%), and horseradish peroxidase (HRP, 0.5 wt%) were obtained by magnetic stirring followed by ultrasonication and then combined with the PCL solution. The C-PCL solution was prepared by dissolving PCL (20 wt%) in the same solvent (DMF:DCM = 1:1), adding curcumin (30 wt% relative to PCL), and mixing under identical conditions. Each solution was loaded into a syringe fitted with a 23G stainless-steel needle and electrospun at 20 kV with a 15 cm tip-to-collector distance and a flow rate of 1.5 mL h^{-1} using an x–y moving electrospinning apparatus (NanoNC, Korea). A single integrated dressing sheet was produced by alternating TGP-PCL and C-PCL layers via cross-continuous deposition.

4.3 | Fabrication of the Multimodal Sensor

The optoelectronic sensor was fabricated on a flexible printed circuit board (fPCB) patterned using a UV laser ablation system (ProtoLaser U4, LPKF, USA). The laser process defined the conductive copper traces for electronic interconnections. On the backside of the fPCB, two pairs of light-emitting diodes (LEDs) and photodiodes were assembled within an 8×8 mm^2 cavity using solder paste (SMDLTLFP10T5, ChipQuik, USA). For glucose dressing quantification, a red LED ($\lambda \approx 625$ nm; LR VH9F-P2R1-1-Z, ams-Osram, USA) was paired with a photodiode (SFH2716, Osram Opto Semiconductors, Germany). For pH measurement, a green LED (LT QH9G-Q2OO-25-2Z4Y, Osram Opto Semiconductors, Germany) was combined with an identical photodiode (SFH2716). In addition, a temperature sensor (NTCG064EF104FTBX, TDK Corporation, Japan) was mounted on the lower surface of the fPCB to measure local wound temperature. To ensure environmental stability, the sensing platform was encapsulated between top and bottom layers of black polydimethylsiloxane (PDMS), shielding the electronics from ambient light and mechanical disturbance. Although the adhesion between polyimide and elastomer substrates is generally poor, sufficient bonding was achieved by a sequential surface-treatment process consisting of oxygen plasma activation for 10 min (Cute-B, Femto Science, South Korea), immersion in 1% (3-mercaptopropyl) trimethoxysilane (MPTMS, 95%, Sigma-Aldrich, USA) methanolic solution for 1 h, followed by epoxy resin coating. This encapsulation process provided both mechanical integrity and robust environmental protection for the sensor.

4.4 | Basic Characteristic of Electrospun TGP-PCL and C-PCL

For morphological characterization of electrospun TGP-PCL and C-PCL fibers, scanning electron microscopy (SEM; Hitachi) was

16163028, 2026, 25, Downloaded from https://advanced.onlinelibrary.wiley.com/doi/10.1002/adfm.202532167 by Korea University Library, Wiley Online Library on [29/03/2026]. See the Terms and Conditions (https://onlinelibrary.wiley.com/terms-and-conditions) on Wiley Online Library for rules of use; OA articles are governed by the applicable Creative Commons License

performed at an accelerating voltage of 5 kV, and fiber diameters were quantified from SEM micrographs using ImageJ. Composite composition was verified by Fourier transform infrared (FTIR) spectroscopy (Thermo Fisher Scientific) in transmission mode over 400–4000 cm^{-1}. Biocompatibility was assessed by a 7-day proliferation assay with NIH 3T3 fibroblasts, and surface adhesion was visualized by SEM. Antimicrobial activity was evaluated over 36 h against Staphylococcus aureus and Escherichia coli.

4.5 | Operation of the NFC Platform

Wireless and battery-free operation was achieved using an NFC microcontroller unit (RF430FRL152H, Texas Instruments, USA) connected to a five-turn copper coil antenna (wire width = 0.2 mm, radius = 15 mm) patterned on the fPCB. The resonant frequency of the antenna was tuned to 13.56 MHz using 68 pF chip capacitors according to the resonance equation.

$$f_0 = \frac{1}{2\pi\sqrt{LC}}$$

A dual-channel micropower operational amplifier (ADA4505-2ARMZ, Analog Devices, USA) amplified the photocurrent signals from the photodiodes. The rectified power port of the NFC MCU provided a constant voltage source, ensuring stable power delivery to all electronic components. The NFC MCU was programmed using the TRF7970AEVM evaluation board (Texas Instruments, USA) through the Code Composer Studio environment (Texas Instruments, USA). Data communication followed the ISO15693 protocol, utilizing an antenna reader (ID ISC. LRM2500-A, FEIG, Germany) or customize smartphone application (Android studio) for wireless energy transfer and signal transmission.

4.6 | Characterization of the Device

The electrical performance of the NFC-based optoelectronic device was characterized using a vector network analyzer (AA-230 Zoom, RigExpert, Ukraine) to evaluate the resonance and impedance response of the antenna circuit. The effect of external light on the sensor output was assessed under controlled illumination conditions using a solar simulator (LAX-C100, Asahi Spectra, USA). Mechanical stability was tested using a universal testing machine (UTM, Shimadzu Corporation, Japan), applying compressive forces of up to 2 N directly onto the sensor surface. Peel tests were conducted using the UTM integrated with a customized linear stage operating at a constant speed of 10 mm s^{-1}. The test was performed at the interface between the packaging layer of the wireless patch and the colorimetric dressings. Adhesion strength was quantified by applying a perpendicular pulling force to the adhesive interface while recording the force required to peel the dressing from the packaging layer.

4.7 | Animal Experiments and In Vivo Evaluation

All animal experiments were conducted in compliance with the institutional and national guidelines for animal care and were approved by the Institutional Animal Care and Use Committee (IACUC) of Caltech (Protocol No. 1800). For the wound model, each rat was anesthetized with isoflurane (2.5 % in O_2), and the dorsal hair was shaved and sterilized using chlorhexidine scrub followed by chlorhexidine solution. To induce postoperative analgesia, ketoprofen (Ketofen; 1:20 dilution, 1 μL g^{-1} body weight), 0.5 % bupivacaine (1:5 dilution, 1 μL g^{-1}), and Ethiqa XR (0.65 mg kg^{-1}) were administered prior to surgery. A full-thickness wound (10 mm diameter) was created on the dorsal skin using surgical scissors. To establish localized infection, 50 μL of Escherichia coli suspension (10^6 CFU mL^{-1} in PBS) was applied directly to the wound site. Following infection induction, a pH-responsive colorimetric dressing was placed over the wound. Except during wireless monitoring sessions, the dressing was covered and secured with a transparent Tegaderm film to maintain contact and protect the wound surface. For glucose sensing, a glucose solution (2 g kg^{-1} body weight, dissolved in sterile saline) was administered via intraperitoneal injection to transiently elevate systemic glucose levels. Colorimetric changes in the dressing were photographed at predetermined time points under identical lighting conditions, and sensor data were transmitted to a computer interface for analysis. Wireless data acquisition during in vivo experiments was performed using the NFC reader and laptop-based interface shown in Figure S16. The NFC reader (ID ISC. LRM2500-A, FEIG, Germany) was connected to a NFC antenna (ID ISC.ANT 310/310, FEIG electronic), enabling wireless power delivery to the patch and real-time data collection from the NFC MCU.

Acknowledgements

This work was supported by the National Research Foundation of Korea (NRF) grant funded by the Korean government (MSIT, No. 2021R1A2C3008742). This research was supported by the Regional Innovation System & Education(RISE) program through the Daejeon RISE Center, funded by the Ministry of Education(MOE) and the Daejeon Metropolitan City, Republic of Korea.(2025-RISE-06-002) This work was supported by Alchemist Project grant funded by Korea Evaluation Institute of Industrial Technology (KEIT) & the Korea Government (MOTIE) (Project Number: 1415179744, 20019169) and by Ministry of Culture, Sports and Tourism and Korea Creative Content Agency (ProjectNumber: RS-2024-00343692).

Conflicts of Interest

The authors declare no conflicts of interest.

Data Availability Statement

The data that support the findings of this study are available from the corresponding author upon reasonable request.

References

1. N. Amin and J. Doupis, "Diabetic Foot Disease: From the Evaluation of the "Foot at Risk" to the Novel Diabetic Ulcer Treatment Modalities," *World Journal of Diabetes* 7 (2016): 153–164, https://doi.org/10.4239/wjd.v7.i7.153.

2. W. J. Jeffcoate and K. G. Harding, "Diabetic Foot Ulcers," *The Lancet* 361 (2003): 1545–1551, https://doi.org/10.1016/S0140-6736(03)13169-8.

3. D. G. Armstrong, T. Tan, A. J. M. Boulton, and S. A. Bus, "Diabetic Foot Ulcers," *Jama* 330 (2023): 62–75, https://doi.org/10.1001/jama.2023.10578.

16163028, 2026, 25, Downloaded from https://advanced.onlinelibrary.wiley.com/doi/10.1002/adfm.202532167 by Korea University Library, Wiley Online Library on [29/03/2026]. See the Terms and Conditions (https://onlinelibrary.wiley.com/terms-and-conditions) on Wiley Online Library for rules of use; OA articles are governed by the applicable Creative Commons License

4. J. B. Rice, U. Desai, A. K. G. Cummings, H. G. Birnbaum, M. Skornicki, and N. B. Parsons, "Burden of Diabetic Foot Ulcers for Medicare and Private Insurers," *Diabetes Care* 37 (2014): 651–658, https://doi.org/10.2337/dc13-2176.

5. Y. Zhang, P. A. Lazzarini, S. M. McPhail, J. J. van Netten, D. G. Armstrong, and R. E. Pacella, "Global Disability Burdens of Diabetes-Related Lower-Extremity Complications in 1990 and 2016," *Diabetes Care* 43 (2020): 964–974, https://doi.org/10.2337/dc19-1614.

6. M. Edmonds, C. Manu, and P. Vas, "The Current Burden of Diabetic Foot Disease," *Journal of Clinical Orthopaedics and Trauma* 17 (2021): 88–93, https://doi.org/10.1016/j.jcot.2021.01.017.

7. D. J. Newton, F. Khan, J. J. F. Belch, M. R. Mitchell, and G. P. Leese, "Blood Flow Changes in Diabetic Foot Ulcers Treated With Dermal Replacement Therapy," *The Journal of Foot and Ankle Surgery* 41 (2002): 233–237, https://doi.org/10.1016/S1067-2516(02)80020-5.

8. J. Kim, "The Pathophysiology of Diabetic Foot: A Narrative Review," *Journal of Yeungnam Medical Science* 40 (2023): 328–334, https://doi.org/10.12701/jyms.2023.00731.

9. X. Wang, C. Yuan, B. Xu, and Z. Yu, "Diabetic Foot Ulcers: Classification, Risk Factors and Management," *World Journal of Diabetes* 13 (2022): 1049–1065, https://doi.org/10.4239/wjd.v13.i12.1049.

10. M. Monteiro-Soares, E. J. Boyko, W. Jeffcoate, et al., "Diabetic Foot Ulcer Classifications: A Critical Review," *Diabetes/Metabolism Research and Reviews* 36 (2020): 3272, https://doi.org/10.1002/dmrr.3272.

11. S. Ono, R. Imai, Y. Ida, D. Shibata, T. Komiya, and H. Matsumura, et al., "Increased Wound pH as an Indicator of Local Wound Infection in Second Degree Burns," *Burns* 41 (2015): 820–824.

12. L. A. Schneider, A. Korber, S. Grabbe, and J. Dissemond, "Influence of pH on Wound-Healing: A New Perspective for Wound-Therapy?" *Archives of Dermatological Research* 298 (2007): 413–420, https://doi.org/10.1007/s00403-006-0713-x.

13. S. L. Percival, S. McCarty, J. A. Hunt, and E. J. Woods, "The Effects of pH on Wound Healing, Biofilms, and Antimicrobial Efficacy," *Wound Repair and Regeneration* 22 (2014): 174–186, https://doi.org/10.1111/wrr.12125.

14. L. Bennison, C. Miller, R. Summers, A. Minnis, G. Sussman, and W. McGuiness, "The pH of Wounds During Healing and Infection: A Descriptive Literature Review," *Wound Practice & Research: Journal of the Australian Wound Management Association* 25 (2020): 63–69.

15. Y. Xiong, S. Knoedler, M. Alfertshofer, et al., "Mechanisms and Therapeutic Opportunities in Metabolic Aberrations of Diabetic Wounds: A Narrative Review," *Cell Death & Disease* 16 (2025): 341, https://doi.org/10.1038/s41419-025-07583-3.

16. S. Patel, S. Srivastava, M. R. Singh, and D. Singh, "Mechanistic Insight Into Diabetic Wounds: Pathogenesis, Molecular Targets and Treatment Strategies to Pace Wound Healing," *Biomedicine & Pharmacotherapy* 112 (2019): 108615, https://doi.org/10.1016/j.biopha.2019.108615.

17. W. McGuiness, E. Vella, and D. Harrison, "Influence of Dressing Changes on Wound Temperature," *Journal of Wound Care* 13 (2004): 383–385, https://doi.org/10.12968/jowc.2004.13.9.26702.

18. R. Derwin, D. Patton, H. Strapp, and Z. Moore, "Wound pH and Temperature as Predictors of Healing: An Observational Study," *Journal of Wound Care* 32 (2023): 302–310, https://doi.org/10.12968/jowc.2023.32.5.302.

19. Manisha, Niharika, P. Gaur, R. Goel, K. Lata, and R. Mishra, "Understanding Diabetic Wounds: A Review of Mechanisms, Pathophysiology, and Multimodal Management Strategies," *Current Reviews in Clinical and Experimental Pharmacology* 20 (2025): 207–228.

20. R. Simman, S. J. Bakewell, D. Bell, S. Shuman, and M. Cheney, "A Novel Approach for the Treatment of Diabetic Foot Ulcers Using a Multimodal Wound Matrix: A Clinical Study," *Journal of Wound Care* 33 (2024): 772–777, https://doi.org/10.12968/jowc.2024.0085.

21. A. Omo-Okhuasuyi, Y. Jin, M. ElHefnawi, Y. Chen, and M. Flores, "Multimodal Identification of Molecular Factors Linked to Severe Diabetic Foot Ulcers Using Artificial Intelligence," *International Journal of Molecular Sciences* 25 (2024): 10686, https://doi.org/10.3390/ijms251910686.

22. M. Smieja, D. L. Hunt, D. Edelman, E. Etchells, J. Cornuz, and D. L. Simel, "Clinical Examination for the Detection of Protective Sensation in the Feet of Diabetic Patients," *Journal of General Internal Medicine* 14 (1999): 418–424, https://doi.org/10.1046/j.1525-1497.1999.05208.x.

23. A. W. Chan, I. A. MacFarlane, D. Bowsher, and J. A. Campbell, "Weighted Needle Pinprick Sensory Thresholds: A Simple Test of Sensory Function in Diabetic Peripheral Neuropathy," *Journal of Neurology, Neurosurgery & Psychiatry* 55 (1992): 56–59, https://doi.org/10.1136/jnnp.55.1.56.

24. A. Raj, K. Sadhana, and K. P. Suhaas, "A Novel Multi-Modal Approach That Fuses Dermoscopic Images With Thermal Imaging in Pre-Emptive Identification of Diabetic Foot Ulcers (DFUs)," *SN Computer Science* 5 (2024): 1055, https://doi.org/10.1007/s42979-024-03439-3.

25. R. Mukherjee, S. Tewary, and A. Routray, "Diagnostic and Prognostic Utility of Non-Invasive Multimodal Imaging in Chronic Wound Monitoring: A Systematic Review," *Journal of Medical Systems* 41 (2017): 46, https://doi.org/10.1007/s10916-016-0679-y.

26. M. Chang, T. Yu, J. Luo, et al., "Multimodal Sensor System for Pressure Ulcer Wound Assessment and Care," *IEEE Transactions on Industrial Informatics* 14 (2018): 1186–1196, https://doi.org/10.1109/TII.2017.2782213.

27. J. Xin, L. Gao, W. Zhang, et al., "A Thermogalvanic Cell Dressing for Smart Wound Monitoring and Accelerated Healing," *Nature Biomedical Engineering* (2025): 1–14, https://doi.org/10.1038/s41551-025-01440-6.

28. B. Mirani, E. Pagan, B. Currie, et al., "An Advanced Multifunctional Hydrogel-Based Dressing for Wound Monitoring and Drug Delivery," *Advanced Healthcare Materials* 6 (2017): 1700718, https://doi.org/10.1002/adhm.201700718.

29. K. Zheng, Y. Tong, S. Zhang, et al., "Flexible Bicolorimetric Polyacrylamide/Chitosan Hydrogels for Smart Real-Time Monitoring and Promotion of Wound Healing," *Advanced Functional Materials* 31 (2021): 2102599, https://doi.org/10.1002/adfm.202102599.

30. S. Wang, W.-Y. Wu, J. C. C. Yeo, et al., "Responsive Hydrogel Dressings for Intelligent Wound Management," *Nature Biomedical Engineering* 1 (2023): 12021.

31. X. Meng, X. Xiao, S. Jeon, et al., "Self-Contracting, Battery-Free Triboelectric Wound Healing Strip With Strong Wet Adhesion," *Nature Communications* 16 (2025): 7220, https://doi.org/10.1038/s41467-025-62312-w.

32. Q. Pang, F. Yang, Z. Jiang, K. Wu, R. Hou, and Y. Zhu, "Smart Wound Dressing for Advanced Wound Management: Real-Time Monitoring and On-Demand Treatment," *Materials & Design* 229 (2023): 111917, https://doi.org/10.1016/j.matdes.2023.111917.

33. R. Dong and B. Guo, "Smart Wound Dressings for Wound Healing," *Nano Today* 41 (2021): 101290, https://doi.org/10.1016/j.nantod.2021.101290.

34. H. Ehtesabi, S. Kalji, and L. Movsesian, "Smartphone-Based Wound Dressings: A Mini-Review," *Heliyon* 8 (2022): 09876.

35. R. Kaveti, M. A. Jakus, H. Chen, et al., "Water-Powered, Electronics-Free Dressings That Electrically Stimulate Wounds for Rapid Wound Closure," *Science Advances* 10 (2024): ado7538, https://doi.org/10.1126/sciadv.ado7538.

36. O. Eskilson, E. Zattarin, L. Berglund, et al., "Nanocellulose Composite Wound Dressings for Real-Time pH Wound Monitoring," *Materials Today Bio* 19 (2023): 100574, https://doi.org/10.1016/j.mtbio.2023.100574.

37. A. A. Arafa, A. A. Nada, A. Y. Ibrahim, M. K. Zahran, and O. A. Hakeim, "Greener Therapeutic pH-Sensing Wound Dressing Based on *Curcuma Longa* and Cellulose Hydrogel," *European Polymer Journal* 159 (2021): 110744, https://doi.org/10.1016/j.eurpolymj.2021.110744.

16163028, 2026, 25, Downloaded from https://advanced.onlinelibrary.wiley.com/doi/10.1002/adfm.202532167 by Korea University Library, Wiley Online Library on [29/03/2026]. See the Terms and Conditions (https://onlinelibrary.wiley.com/terms-and-conditions) on Wiley Online Library for rules of use; OA articles are governed by the applicable Creative Commons License

38. J. Ha, Y. Jeong, J. Ahn, et al., "A Wearable Colorimetric Sweat pH Sensor-Based Smart Textile for Health State Diagnosis," *Materials Horizons* 10 (2023): 4163–4171, https://doi.org/10.1039/D3MH00340J.

39. B. Mirani, Z. Hadisi, E. Pagan, et al., "Smart Dual-Sensor Wound Dressing for Monitoring Cutaneous Wounds," *Advanced Healthcare Materials* 12 (2023): 2203233, https://doi.org/10.1002/adhm.202203233.

40. J. Ha, J. Y. Kim, D. Kim, et al., "Multifunctional Micro/Nanofiber Based-Dressing Patch With Healing, Protection, and Monitoring Capabilities for Advanced Wound Care," *Advanced Materials Technologies* 8 (2023): 2201765, https://doi.org/10.1002/admt.202201765.

41. S. Cho, J. Ha, J. Ahn, et al., "Wireless, Battery-Free, Optoelectronic Diagnostic Sensor Integrated Colorimetric Dressing for Advanced Wound Care," *Advanced Functional Materials* 34 (2024): 2316196, https://doi.org/10.1002/adfm.202316196.

42. J. Miao, H. Chai, L. Song, et al., "A pH-Responsive Anthocyanin-Based Hydrogel With Colorimetric Infection Monitoring and Antibacterial Properties for Wound Healing," *Journal of Materials Chemistry B* (2026).

43. X. T. Zheng, Z. Yang, L. Sutarlie, et al., "Battery-Free and AI-Enabled Multiplexed Sensor Patches for Wound Monitoring," *Science Advances* 9 (2023): adg6670, https://doi.org/10.1126/sciadv.adg6670.

44. C. Wang, E. Shirzaei Sani, and W. Gao, "Wearable Bioelectronics for Chronic Wound Management," *Advanced Functional Materials* 32 (2022): 2111022, https://doi.org/10.1002/adfm.202111022.

45. C. Wang, E. Shirzaei Sani, C. Shih, et al., "Wound Management Materials and Technologies From Bench to Bedside and Beyond," *Nature Reviews Materials* 9 (2024): 550–566, https://doi.org/10.1038/s41578-024-00693-y.

46. Y. Gao, D. T. Nguyen, T. Yeo, et al., "A Flexible Multiplexed Immunosensor for Point-of-Care in Situ Wound Monitoring," *Science Advances* 7 (2021): abg9614, https://doi.org/10.1126/sciadv.abg9614.

47. C. Wang, K. Fan, E. Shirzaei Sani, et al., "A Microfluidic Wearable Device for Wound Exudate Management and Analysis in Human Chronic Wounds," *Science Translational Medicine* 17 (2025): adt0882, https://doi.org/10.1126/scitranslmed.adt0882.

48. M. Li, W. Xia, Y. M. Khoong, et al., "Smart and Versatile Biomaterials for Cutaneous Wound Healing," *Biomaterials Research* 27 (2023): 87, https://doi.org/10.1186/s40824-023-00426-2.

49. Y. Jiang, A. A. Trotsyuk, S. Niu, et al., "Wireless, Closed-Loop, Smart Bandage With Integrated Sensors and Stimulators for Advanced Wound Care and Accelerated Healing," *Nature Biotechnology* 41 (2023): 652–662, https://doi.org/10.1038/s41587-022-01528-3.

50. J. Wang, Y. Luo, Z. Zhou, J. Xiao, T. Xu, and X. Zhang, "Epidermal Wearable Optical Sensors for Sweat Monitoring," *Communications Materials* 5 (2024): 77, https://doi.org/10.1038/s43246-024-00518-z.

51. Z. Wang, Y. Dong, X. Sui, et al., "An Artificial Intelligence-Assisted Microfluidic Colorimetric Wearable Sensor System for Monitoring of Key Tear Biomarkers," *npj Flexible Electronics* 8 (2024): 35, https://doi.org/10.1038/s41528-024-00321-3.

52. N. T. Garland, J. W. Song, T. Ma, et al., "A Miniaturized, Battery-Free, Wireless Wound Monitor That Predicts Wound Closure Rate Early," *Advanced Healthcare Materials* 12 (2023): 2301280.

53. E. Shirzaei Sani, C. Xu, C. Wang, et al., "A Stretchable Wireless Wearable Bioelectronic System for Multiplexed Monitoring and Combination Treatment of Infected Chronic Wounds," *Science Advances* 9 (2023): adf7388, https://doi.org/10.1126/sciadv.adf7388.

54. M. Li, C. Wang, Q. Yu, et al., "A Wearable and Stretchable Dual-Wavelength LED Device for Home Care of Chronic Infected Wounds," *Nature Communications* 15 (2024): 9380, https://doi.org/10.1038/s41467-024-53579-6.

55. X. Zhao, J. Huang, J. Zhang, et al., "Soft Bioelectronics Embedded With Self-Confined Tetrahedral DNA Circuit for High-Fidelity Chronic Wound Monitoring," *Nature Communications* 16 (2025): 8899, https://doi.org/10.1038/s41467-025-63927-9.

56. Z. Xiong, S. Achavananthadith, S. Lian, et al., "A Wireless and Battery-Free Wound Infection Sensor Based on DNA Hydrogel," *Science Advances* 7 (2021): abj1617, https://doi.org/10.1126/sciadv.abj1617.

57. Y. S. Oh, J. Kim, Z. Xie, et al., "Battery-Free, Wireless Soft Sensors for Continuous Multi-Site Measurements of Pressure and Temperature From Patients at Risk for Pressure Injuries," *Nature Communications* 12 (2021): 5008, https://doi.org/10.1038/s41467-021-25324-w.

58. S. Kim, Y. S. Oh, K. Lee, et al., "Battery-Free, Wireless, Cuff-Type, Multimodal Physical Sensor for Continuous Temperature and Strain Monitoring of Nerve," *Small* 19 (2023): 2206839, https://doi.org/10.1002/smll.202206839.

59. H. Han, Y. S. Oh, S. Cho, et al., "Battery-Free, Wireless, Ionic Liquid Sensor Arrays to Monitor Pressure and Temperature of Patients in Bed and Wheelchair," *Small* 19 (2023): 2205048, https://doi.org/10.1002/smll.202205048.

60. H. Han, H. Kim, S. Cho, et al., "Wireless, Battery-Free Multi-Axial Sensor for Augmented Reality-Assisted Monitoring at Skin Interfaces," *npj Flexible Electronics* 9 (2025): 102, https://doi.org/10.1038/s41528-025-00479-4.

61. S. Cho, H. Han, H. Park, et al., "Wireless, Multimodal Sensors for Continuous Measurement of Pressure, Temperature, and Hydration of Patients in Wheelchair," *npj Flexible Electronics* 7 (2023): 8, https://doi.org/10.1038/s41528-023-00238-3.

Supporting Information

Additional supporting information can be found online in the Supporting Information section.

Supporting file 1: adfm73945-sup-0001-SuppMat.docx. **Supporting file 2**: adfm73945-sup-0002-VideoS1.mp4. **Supporting file 3**: adfm73945-sup-0003-VideoS2.mp4.

16163028, 2026, 25, Downloaded from https://advanced.onlinelibrary.wiley.com/doi/10.1002/adfm.202532167 by Korea University Library, Wiley Online Library on [29/03/2026]. See the Terms and Conditions (https://onlinelibrary.wiley.com/terms-and-conditions) on Wiley Online Library for rules of use; OA articles are governed by the applicable Creative Commons License